AFRL-OSR-VA-TR-2013-0395

(YIP 10) - BIO-INSPIRED INTERFACES FOR HYBRID STRUCTURES

Ashkan Vaziri

Northeastern University

JULY 2013
Final Report

AIR FORCE RESEARCH LABORATORY
AF OFFICE OF SCIENTIFIC RESEARCH (AFOSR)
ARLINGTON, VIRGINIA 22203
AIR FORCE MATERIEL COMMAND

REPORT DOCUMENTATION PAGE

The public reporting burden for this collection of information is estimated to average 1 hour per response, including the time for reviewing instructions, searching existing data sources, gathering and maintaining the data needed, and completing and reviewing the collection of information. Send comments regarding this burden estimate or any other aspect of this collection of information, including suggestions for reducing the burden, to the Department of Defense, Executive Services and Communications Directorate (0704-0188). Respondents should be aware that notwithstanding any other provision of law, no person shall be subject to any penalty for failing to comply with a collection of information if it does not display a currently valid OMB control number.

PLEASE DO NOT RETURN YOUR FORM TO THE ABOVE ORGANIZATION.

1. REPORT DATE *(DD-MM-YYYY)*	2. REPORT TYPE	3. DATES COVERED *(From - To)*

4. TITLE AND SUBTITLE

5a. CONTRACT NUMBER

5b. GRANT NUMBER

5c. PROGRAM ELEMENT NUMBER

6. AUTHOR(S)

5d. PROJECT NUMBER

5e. TASK NUMBER

5f. WORK UNIT NUMBER

7. PERFORMING ORGANIZATION NAME(S) AND ADDRESS(ES)

8. PERFORMING ORGANIZATION REPORT NUMBER

9. SPONSORING/MONITORING AGENCY NAME(S) AND ADDRESS(ES)

10. SPONSOR/MONITOR'S ACRONYM(S)

11. SPONSOR/MONITOR'S REPORT NUMBER(S)

12. DISTRIBUTION/AVAILABILITY STATEMENT

13. SUPPLEMENTARY NOTES

14. ABSTRACT

15. SUBJECT TERMS

16. SECURITY CLASSIFICATION OF:			17. LIMITATION OF ABSTRACT	18. NUMBER OF PAGES	19a. NAME OF RESPONSIBLE PERSON
a. REPORT	b. ABSTRACT	c. THIS PAGE			
					19b. TELEPHONE NUMBER *(Include area code)*

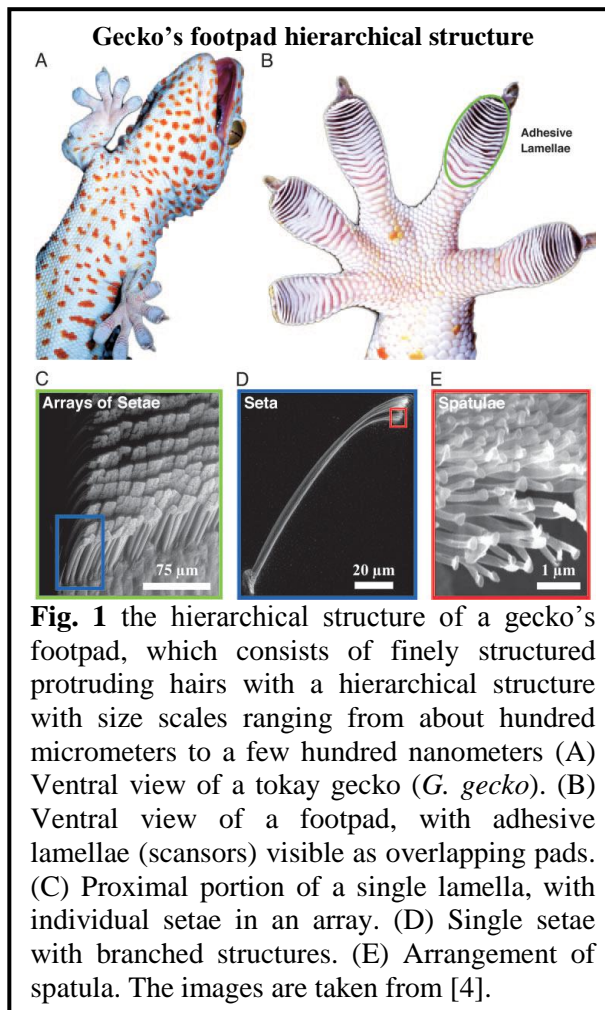# (YIP 10) - BIO-INSPIRED INTERFACES FOR HYBRID STRUCTURES
PI: Ashkan Vaziri – Northeastern University
Final Report

1. Introduction

The constituents of biological materials generally have different compositions, shapes, sizes, and spatial distributions leading to a complex hierarchical organization that is found in many structural biological materials, such as wood, vertebrate bones and teeth, mollusk shells and arthropod exoskeletons [1, 2]. Two interesting examples of such biological systems are gecko's footpad (Figure 1) and mother-of-pearl or nacre. Each of these biological systems presents a unique example of the role of structural hierarchy and heterogeneity in achieving superior material properties and performance at macro scale, which are indeed critical for the system function. The gecko's footpad is one of the most effective adhesion systems found in nature, giving gecko lizards the ability to efficiently climb on both smooth and rough surfaces [3-9]. Nacre, on the other hand, has material properties and toughness that are far superior to its material ingredient constituents. The nacre structure is mostly composed of microscopic ceramic tablets densely packed and bonded together by a thin layer of biopolymer [10-12]. The tablets are found to have wavy surfaces [12-14] with the smallest features at the nanoscale: the surface of tablets are fashioned with nanoasperities,

Gecko's footpad hierarchical structure

Fig. 1 the hierarchical structure of a gecko's footpad, which consists of finely structured protruding hairs with a hierarchical structure with size scales ranging from about hundred micrometers to a few hundred nanometers (A) Ventral view of a tokay gecko (*G. gecko*). (B) Ventral view of a footpad, with adhesive lamellae (scansors) visible as overlapping pads. (C) Proximal portion of a single lamella, with individual setae in an array. (D) Single setae with branched structures. (E) Arrangement of spatula. The images are taken from [4].

which are aragonite grains with crystallographic orientation normal to the plane of the tablets [11, 15-18]. The hierarchical microstructure of this biological material is the result of millions of years of evolution, leading to its superior strength and toughness compared to the ceramic it is made of [12-16]. Many other biological material systems have also a similar structure and are essentially made of ceramic building blocks with polymeric matrices that form nanocomposite materials with many interfaces at different scales. Examples include mineralized tissues of vertebrates, such as bone, teeth, and calcified tendons and the cuticle of the lobster *Homarus americanus* [19-21]. A critical aspect of performance of these materials is the superior properties of their interfaces, which is indeed known to be responsible for their remarkable material properties.

In this project, we used our expertise in structural mechanics and materials science to study the fundamental behavior of bio-inspired surfaces and interface configurations, using robust experiments at both micro and macro scale, combined with theoretical analysis and detailed numerical simulations of surface behavior and interfacial failure. In addition, we

investigated the behavior and properties of a new class of hierarchical honeycombs with self-similar architecture. The details of our investigations are discussed below and in more details in the following sections:
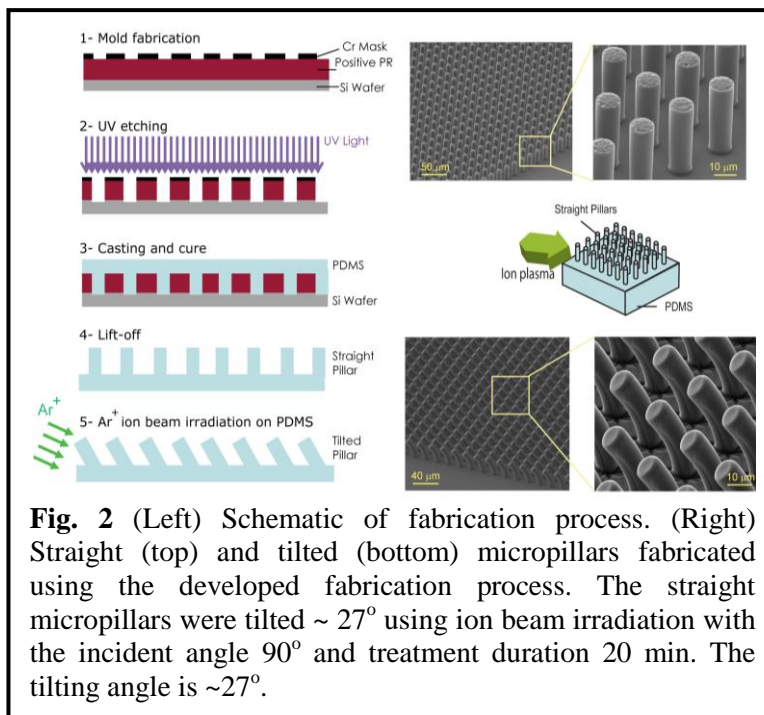
Bioinspired surfaces: The foot of many of insects and lizards is covered by intricate fibrillar structures that are responsible for their superb maneuvering ability. Among these creatures, gecko lizards have one of the most efficient and interesting adhesion devices consisting of finely angled arrays of branched fibers (See Fig. 1). In this part of the project, we collaborated with the Convergence Technology Laboratory at the Korea Institute of Science and Technology to develop surfaces with biologically-inspired topologies. The efforts includes development of a method to create tilted Janus (two-face) micropillars on the surface of an elastomeric polymer to mimic the geometry of gecko's footpad. We performed a set of experiments to measure the adhesion and friction characteristics and other mechanical properties of the developed bioinspired surfaces.

Interfaces with Extreme topology and geometry: Lightweight materials are widely used in the design of marine and aerospace structures where strength-to-weight ratio is a critical design factor. Many of these structures must achieve diverse – and often divergent – properties and function, and thus are made from dissimilar materials which might have very different properties. Such *hybrid structures* can minimize weight by using the lowest density material with the appropriate strength, stiffness or ductility in each area of the structural assembly. But a resulting key challenge of hybrid structures is joint performance and its integrity during the service life of the structure. In this project, the effects of interface morphology on inelastic elongation, crack initiation and arrest, and energy absorption of geometrically different adhesively bonded single lap joints were investigated. Our study includes fabricating and testing bonded lap joints with different interface morphologies, along with detailed finite element modeling. Our findings provide insight for the development of robust multi-material and multi-component structural systems with tailorable properties, and for understanding the role of interface morphology in some biological systems.

Self-Similar Hierarchical Honeycombs: Hierarchical structures are observed in nature, and are shown to offer superior efficiency. However, the potential advantages of structural hierarchy are not well understood. In this part of the project, we extensively explored a bending-dominated model material (i.e. transversely loaded hexagonal honeycomb) which is susceptible to improvement by simple iterative refinement that replaces each three-edge structural node with a smaller hexagon. Using a blend of analytical and numerical techniques, both elastic and plastic properties were explored over a range of loadings and iteration parameters. A wide variety of specific stiffness and specific strengths (up to fourfold increase) were achieved. Our study is unique in exploring, partly analytically and partly numerically, a substantial region of parameter space. This includes length and thickness substitution ratios up to fourth order of hierarchy, and the entire range of principal stress ratios. Beyond the specific improvements afforded by this particular case of hierarchical refinement, we suggest that this comprehensive study which involves a truly iterative substitution scheme may serve as a useful illustration of hierarchical behaviour. The findings of this study therefore suggest new avenues for the understanding and development of novel materials and structures with desirable and perhaps actively tailorable properties.

2. Bioinspired Surfaces

Asymmetric adhesion is used by many insects and gecko lizards in nature, allowing them to move on nearly any surface - horizontal or vertical and even at inverted position. In this context, gecko's footpad has attracted significant attention due to its efficiency, superb functionality and sustainability via self-cleaning [22-29]. In this work, we developed a simple technique for fabrication of tilted micropillars that mimics gecko's footpad structure. Figure 2 (left) shows schematics of the five steps involved in creation of the tilted micropillars. In this technique, first, straight micropillars are fabricated on the surface of the

Fig. 2 (Left) Schematic of fabrication process. (Right) Straight (top) and tilted (bottom) micropillars fabricated using the developed fabrication process. The straight micropillars were tilted ~ 27° using ion beam irradiation with the incident angle 90° and treatment duration 20 min. The tilting angle is ~27°.

polydimethylsiloxane (PDMS) using soft lithography (steps 1-4 in Fig. 2). After fabrication of the straight pillars, Ar+ broad ion beam irradiation is used to tilt the micropillars. The outcome is an array of micropillars that are uniformly tilted towards the ion beam irradiation direction. Figure 2 (right) shows the polymer micropillars prior (top) to and after (bottom) 20 min exposure to ion beam with incident angle 90° (parallel to the surface of the polymeric substrate). The micropillars have diameter 9.3 μm, height 30 μm and spacing 10 μm, where spacing is defined as the distance between the edges of the adjacent micropillars (e.g. center to center distance of micropillars in this case is 19.3 μm) – this gives the density of ~ $2700/mm^2$, which is approximately five times lower than the setae density on the gecko's footpad [3, 28, 30]. The developed technique can be used to fabricate micropillars with a wide range of dimensions and spacing with the lower limit of spacing and diameter of ~1 μm [31]. Our work complements previous efforts for fabricating fibrillar structures [29, 32-36], which provided structural organizations that successfully mimic some of the intricate properties of gecko's footpad under controlled experimental conditions. Potential applications of the created structures are vast and range from non-wetting painting and smart adhesives [35-41] to intricate bioinspired designs such as nano- and micro- robotics with climbing abilities [42, 43].

2.1 Fabrication Method

Uniform straight micropillars were created using soft lithography. First, the SU-8 of photoresist (PR) on Si wafer was spin-coated with 30 μm Cr mask and used to fabricate the negative shape of pattern mask (Fig. 2 – step 1). The wafer was heated on a hot plate for 10 min in two steps at 60 °C and 90 °C. Cr masks were placed on solidified PR, aligned with EVG 6200 Mask Aligner and exposed to UV (EVGroup, Austria). Exposed PR were developed and cleaned with isoprofilalcohol. PDMS networks were prepared by mixture of elastomer and cross-linker in mass ratio of 10:1 (Sylgard-184, Dow Corning, MI) and were poured on a pre-patterned
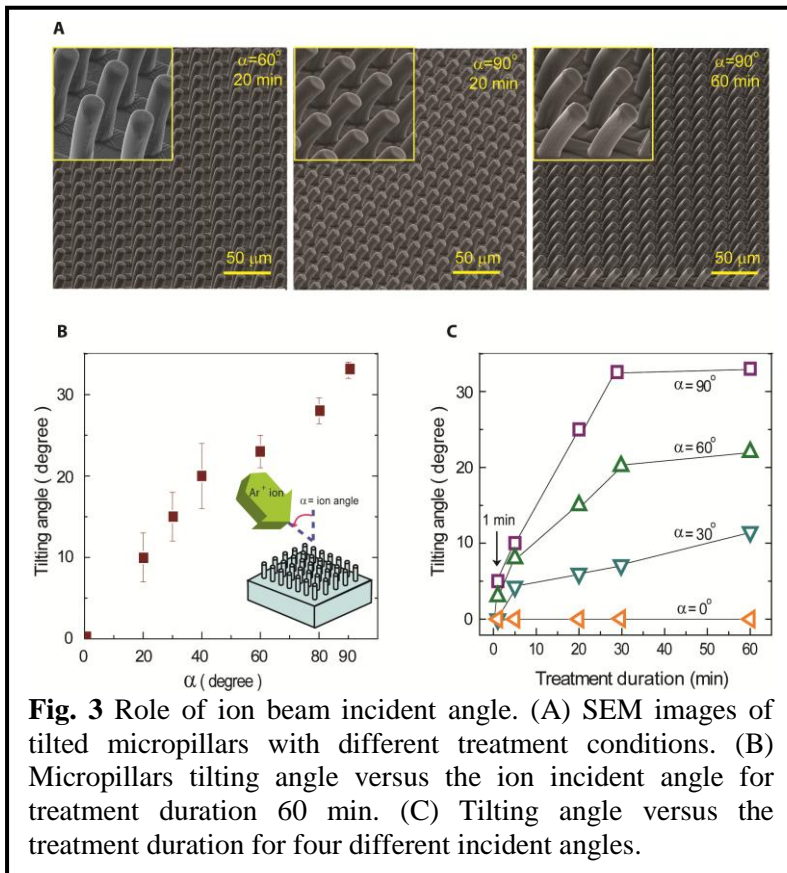
photoresist (PR) mask (Fig. 2 – step 3). The trapped air bubbles were removed in a vacuum chamber. The samples were cured on a hot plate at 75$^{\mathrm{o}}$C for 75 min, resulting in cross-linked PDMS network with straight micropillars (Fig. 2 – step 4). Microscopic images of micropillar structures were acquired using a scanning electron microscope (SEM).

The straight micropillars were subject to Ar$^+$ ion beam irradiation using a hybrid ion beam system (Fig. 2 – Step 5). In this experiment, PDMS substrates with straight micropillars fabricated on their surface were placed on a tilted die at a certain angle in the vacuum chamber. The chamber had the working pressure ~10^{-5} Pa. The ion beam treatment was

Fig. 3 Role of ion beam incident angle. (A) SEM images of tilted micropillars with different treatment conditions. (B) Micropillars tilting angle versus the ion incident angle for treatment duration 60 min. (C) Tilting angle versus the treatment duration for four different incident angles.

made with argon discharge at anode voltage 1 keV, a bias voltage –600 V and a pressure 0.49 Pa. In Figure 3, we studied the role of ion beam incident angle on the tilting angle of the micropillars. Figure 3A shows examples of the tilted pillars subjected to two different ion beam incident angles, 60$^{\mathrm{o}}$ and 90$^{\mathrm{o}}$. Figure 3B shows the dependence of micropillar's tilting angle on the ion incident angle denoted by α for ion treatment of 60 min. Figure 3C expands these results for various treatment durations. Ion beam irradiation normal to the micropillars and parallel to the surface (i.e. $\alpha = 90^{\mathrm{o}}$) leads to the largest tilting angle, while ion beam irradiation normal to the polymer surface and parallel to the straight micropillars (i.e. $\alpha = 0^{\mathrm{o}}$) results in almost no tilting of the micropillars. The examination of the morphology of the tilted pillars indicates that the height of micropillars, where surface wrinkles appear, depends on the ion incident angle. For large incident angles, surface wrinkles appear along the total height of the micropillars, as shown for $\alpha=90^{\mathrm{o}}$ in 3A. For smaller ion incident angles, surface wrinkles appear only on the upper part of the micropillars as the bottom part of the pillars does not get exposed to direct ion beam due to the shadowing effect of other micropillars. This leads to a smaller tilting angle at a lower ion beam incident angle.
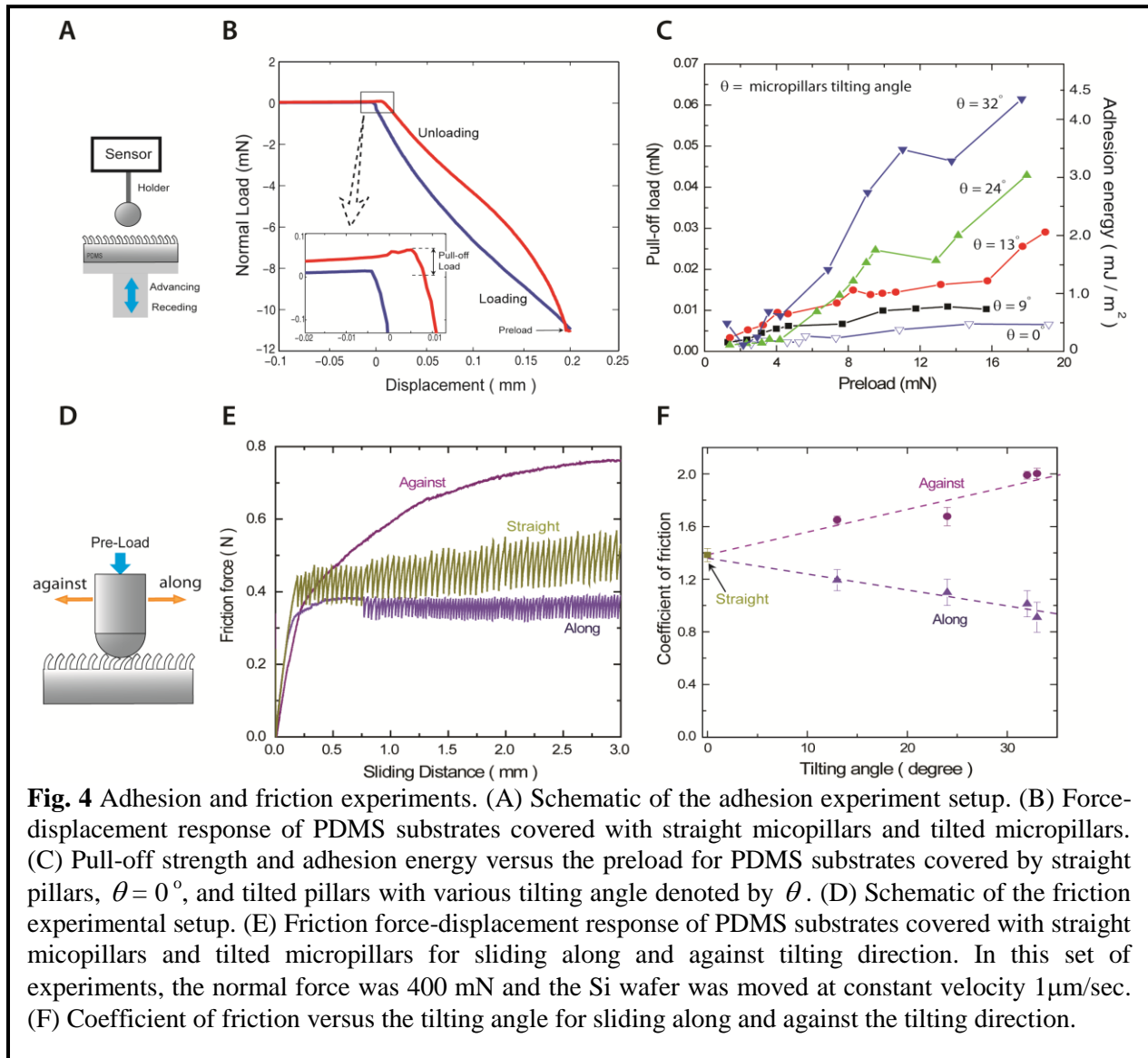
2.2 Adhesion and Friction Experiments

The constant force of micropillars against a steel ball was measured using a tensiometer (DCAT 21, Dataphysics, Germany). In the experiments, first, the stage was moved upward and a 40×40 mm^2 PDMS coupon got in contact with the steel ball with a diameter 6 mm - See Fig. 4A. The stage then moved upward at constant speed 10 µm/s while the force was measured at a frequency 50 Hz by a sensor at a resolution of 1µN. As the force reached a predefined load, or

preload, the stage was set to move downward at a constant speed 10 μm/s, while the forced was measured using by the sensor. The maximum value of positive force denotes the pull-off strength of the surface – see Figure 4B and its inset. In the results shown in Fig. 4B, the maximum preload ~ 11 mN is reached at the maximum advancing displacement of 0.2 mm and the pull-off load is ~ 0.05 mN for micropillars with tilting angle 32°. The pull-off strength of titled micropillars depends on the value of preload and micropillars tilting angle as quantified in Fig. 4C. The results for the straight pillars are also shown in the same figure. In this set of experiments, the tilting angle of micropillars was controlled by changing the treatment duration, while the preload is varied by changing the receding displacement. In general, the pull-off strength of a substrate covered by micropillars increases by increasing the preload and is higher for micropillars with a larger tilting angle. These observations are in qualitative agreement with the sliding-induced adhesion study carried out on the stiff polymer fiber arrays [44]. The equivalent adhesion energy/area, w_{ad}, between the steel ball and a micropillar array can be estimated using the Johnson-Kendall-Robert (JKR) model in Fig. 4C. The results show that the polymer substrate covered by titled micropillars with tilting angle 32°, has an adhesion energy

Fig. 4 Adhesion and friction experiments. (A) Schematic of the adhesion experiment setup. (B) Force-displacement response of PDMS substrates covered with straight micopillars and tilted micropillars. (C) Pull-off strength and adhesion energy versus the preload for PDMS substrates covered by straight pillars, $\theta = 0^{o}$, and tilted pillars with various tilting angle denoted by θ. (D) Schematic of the friction experimental setup. (E) Friction force-displacement response of PDMS substrates covered with straight micopillars and tilted micropillars for sliding along and against tilting direction. In this set of experiments, the normal force was 400 mN and the Si wafer was moved at constant velocity 1μm/sec. (F) Coefficient of friction versus the tilting angle for sliding along and against the tilting direction.

that is about one order larger than the adhesion energy of substrates covered by straight pillars with the same geometry and density.

Directional friction behavior of the tilted micropillars against a Si wafer coupon with 10×10 mm^2 was measured using a custom-made device shown schematically in Fig. 4D. Prior to each experiment, the Si wafer was cleaned with isopropanol. The friction force of a PDMS coupon covered by straight or tilted micropillars was measured at a frequency 64 Hz using a sensor at a resolution of 50μN as the wafer slides. Sliding distance was set 1 mm at the constant speed of 1 μm/sec. The measured friction force was divided by the normal force to estimate the average coefficient of friction at the plateau-region in the steady sliding regime.

In the second experiment, directional friction behavior of the tilted micropillars against a Si wafer was measured using a custom-made setup shown schematically in Figure 4D. The friction force was measured by moving the Si wafer *along* and *against* the tilted pillar direction and was compared to the friction force of straight pillars in Fig. 4E. At the early stage of experiment, the friction force for sliding against the tilting direction was relatively higher than the friction force of straight pillars, as the contact area increases by the sliding displacement. After this initial stage, the friction force was considerably lower when sliding occurs against the pillar direction compared to the friction force of straight pillars and sliding along the pillar direction under the same test condition. This observation is consistent with the observed behavior of gecko's footpad [45, 46], as well as the measurement on biologically inspired synthetic fibrillar surfaces [32, 46]. The fiction force for sliding along the pillar direction is comparable to the friction force of the straight micropillars, however the sliding displacement associated with the steady sliding is shorter for straight pillars compared to sliding along the pillar direction, which is also consistent with previous observations on fibrillar surfaces [33, 46].

The direction dependant friction behavior of titled pillars is further studied in Fig. 4F, where we have estimated the coefficient of friction (COF) of the substrates for various tilting angles of micropillars by dividing the average friction force by the normal force in the the steady sliding regime. The friction force along the tilting direction is about three times higher than the friction force associated with sliding against the tilting direction of micropillars. For this sliding velocity, no significant sensitivity to the tilting angle was observed and the friction force for sliding along the tilting direction of micropillars is comparable with the straight pillars for all tilting angles. We carried out the friction experiment for a wide range of sliding velocities – see the supplementary material. Our results show that the COF for sliding along the tilting direction of micropillars minimally depends on the sliding velocity, which is consistent with the behavior observed for stiff polymer fiber arrays [44]. In contract, the COF for sliding against the micropillar tilting direction decreases remarkably at higher sliding velocities. Sliding against the titling direction is accompanied by significant mechanical deformation of micropillars and thus, the inherent time-dependant behavior (i.e. visco-elasticity) of polymeric micropillars influence the friction behavior of the micropillars, leading to a strongly rate dependant behavior.

3. Bonded joints with extreme topology and geometry

Where structural materials join together, geometrical or elastic discontinuities generally lead to a complex state of deformation and concentrated stresses, which may encourage cracks and defects to initiate and propagate along the bonded joint. The challenge of joint design is especially pronounced for non-metallic structures, since traditional ductile attachment techniques (e.g., welding or brazing) cannot generally be employed. Adhesive properties have been shown to be the limiting factor in many bonded systems [47-50]. This has stimulated the development of better adhesives and bonding procedures [51-53]. Another promising avenue for enhancing bond properties is to tailor the surface morphology. For example, bonded wavy lap joints are shown to have higher strength compared to their counterpart flat lap joint [54-57]. In this project, we extended these studies by introducing extreme morphological and geometrical changes to the bonded lap joint design [58-63]. It was hypothesized that strength and ductility could both be enhanced by changing the bonded region topography.

For our experiments (section 3.1), we fabricated standard flat joints as well as joints with two mirror-image zigzag surface morphologies, and measured the tensile behavior up to failure. The experiments themselves were not intended to explore extensive parameter variations, but rather to benchmark and validate the associated finite element (FE) modeling. It was observed that each kind of non-flat interface morphology displays a characteristic and explainable load-displacement curve, with an initial cracking or debonding event, and followed by rapid crack propagation or arrest depending on the interface morphology. A particular geometry was identified as offering twofold to threefold greater resistance to fracture initiation than the experimentally evaluated non-flat geometries, and thus by implication, greater ultimate strength than the standard flat lap joint. In section 3.2, linear-elastic FE analysis using ABAQUS was employed to evaluate distributions of stress and strain in all the experimental geometries. Also FE simulations were used to obtain the optimized geometrical parameters resulting in the largest strength and load capacity.

3.1 Experimental Investigations

Adherends with three different profiles were machined from 1018 CR steel bar with the following assumed properties: Young's modulus, E_S = 200 GPa, Poisson ratio 0.3, and tensile yield strength 386 MPa. The adherends' length d, width w, and average height h were 120 mm, 3 mm, and 15 mm, respectively. Standard flat joints, as well as two non-flat types with a v-shaped tooth and the matching v-shaped notch (or negative tooth) on each adherend were fabricated and tested. The two non-flat types of adherends are as follows: 1) "Positive" then negative tooth" adherend defined by each adherend becoming thicker (i.e., a tooth) as it enters the joint region. This morphology is frequently denoted by '/\' or 'first point upward' in the report. 2) "Negative then positive tooth" adherend defined by each adherend becoming thinner (i.e. a notch) as it enters the joint region. This morphology is frequently denoted by '\/' or 'first point downward' in the report.

Figure 5A provides a generic description of joint geometry. Interface morphology is defined by an overlap distance L (the projected bond length), first-tooth slope angle θ, and tooth height A (from which is derivable total tooth width $B = 4A/tan(\theta)$). Then flat, /\, and \/ joints correspond to θ & $A = 0$; θ & $A > 0$; and θ & $A < 0$, respectively. We defined the geometry in non-dimensional terms through the tooth height to adherend height ratio (A / h), the total tooth width to total overlap distance ratio (B / L), and the initial angle (θ) of the joint surface. When

teeth are present, the outer tooth flanks, the inner flanks, and the flat between them are named regions III, II and I respectively, as shown in Fig. 5A.
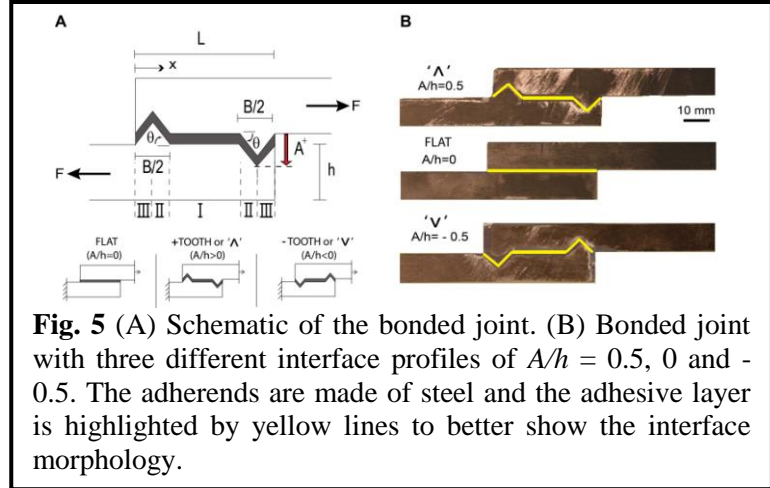

Fig. 5 (A) Schematic of the bonded joint. (B) Bonded joint with three different interface profiles of A/h = 0.5, 0 and -0.5. The adherends are made of steel and the adhesive layer is highlighted by yellow lines to better show the interface morphology.

To fabricate the specimens, pairs of matching adherend types were bonded together using Emerson & Cuming "ECCOBOND G909" adhesive. This is a one-component (no mixing required) heat-curing epoxy with excellent peel strength, and high tensile and shear strengths, designed for metal assemblies such as copper and aluminum. The cured adhesive has Young's modulus, E = 2 GPa (the manufacturer's value was confirmed by uniaxial test of an adhesive bar), Poisson ratio 0.4, and a nominal bond thickness of 1 mm. The adherends overlapped by L = 40 mm, leading to an overall bonded-specimen length of 200 mm. The adherends were machined to fit together with essentially no gaps, then were separated by 1.0 mm to provide clearance for the adhesive. (Depending on local bond-surface angle θ, the epoxy thickness was thus equal to (1.0 mm) $\times cos\theta$.) The surfaces to be bonded were cleaned by alcohol prior to assembly in a bonding jig. Following supplier instructions, the specimens were cured in an oven for 20 minutes at 150° C, then post-cured at room temperature for 2 hours. The unwanted residual adhesive on the specimen was removed carefully by grinding, creating a bond-end adhesive fillet radius of approximately 0.8 mm in the re-entrant corners.

A total of 21 specimens – 7 for each interface type illustrated in Figure 5A – were fabricated and tested. The specimens with non-flat geometries had B / L = 0.5 (total tooth width being half the 40 mm specimen overlap). For '/\' morphology, A / h = 0.5 (a tooth protruding 5 mm from the adherend where it begins the overlap), while for '\/' morphology, A / h = - 0.5 (a 'negative tooth' or notch with adherend material removed to a depth of 5 mm). The angles θ in the two cases are $\pm$ 45 degrees. Enlarged illustrations of the three joint types are shown in Figure 5B.

Uniaxial tensile tests were performed on an INSTRON 5582 universal testing machine at a displacement rate of 1 mm / min. For the tensile test, approximately 12 mm at each end was gripped, leaving 176 mm between testing grips. One rigid grip, and one self-aligning grip with its pivot 280 mm from the grip face, contacted the specimens on the 15 mm wide faces visible in the figures (not the 3 mm 'top and bottom' faces). Since only one of the grips was self-aligning, the load's line of action was not completely within the bond plane. However, the magnitude of moment about the bond center was estimated to be minimal (equivalent in the elastic regime to a lateral displacement of the load line by just 0.75 mm, which can be neglected).
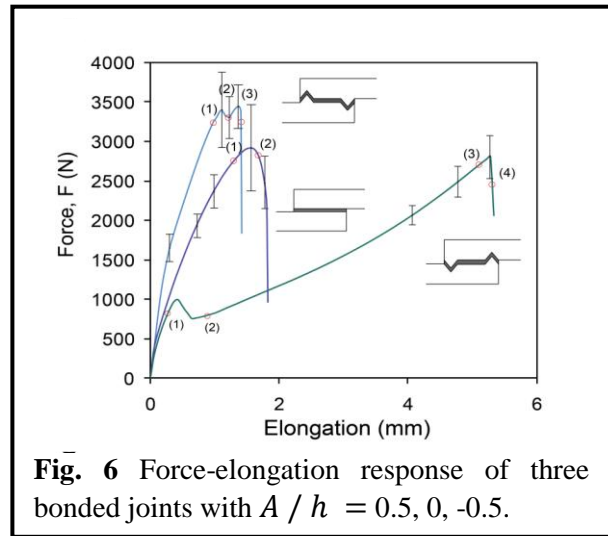
Figure 6 shows measured applied-force versus elongation results. Each curve represents a typical response for each specimen type, with range bars indicating the greatest and least load measured at specific elongations. Clearly, the three types of joint differ significantly in their mechanical response. For the non-flat specimens, the 'first bond failure' (indicated as stage 2) probably occurs due to normal stress across the adhesive bond, as will be further discussed in section 3. For the '/\' specimens, the initial crack development occurs in the pair of regions II at a

load of approximately 3300 N (corresponding to far-field adherend tensile stress of 110 MPa). However for '∨' specimens, the initial cracks develop at the adherend-adhesive interface at the outer edges of the bond (i.e., regions III), at a load around 800 N.

Fig. 6 Force-elongation response of three bonded joints with $A / h = 0.5, 0, -0.5$.

After initial failure in non-flat joints, the specimen types respond differently to further elongation. For '∧' specimens, after the initial occurrence of cracks in regions II, propagation is slightly delayed by the change of interface slope between regions II and I. This results in a slight increase in the load resistance of the specimen, which may be identified by a second distinct peak in the load-displacement r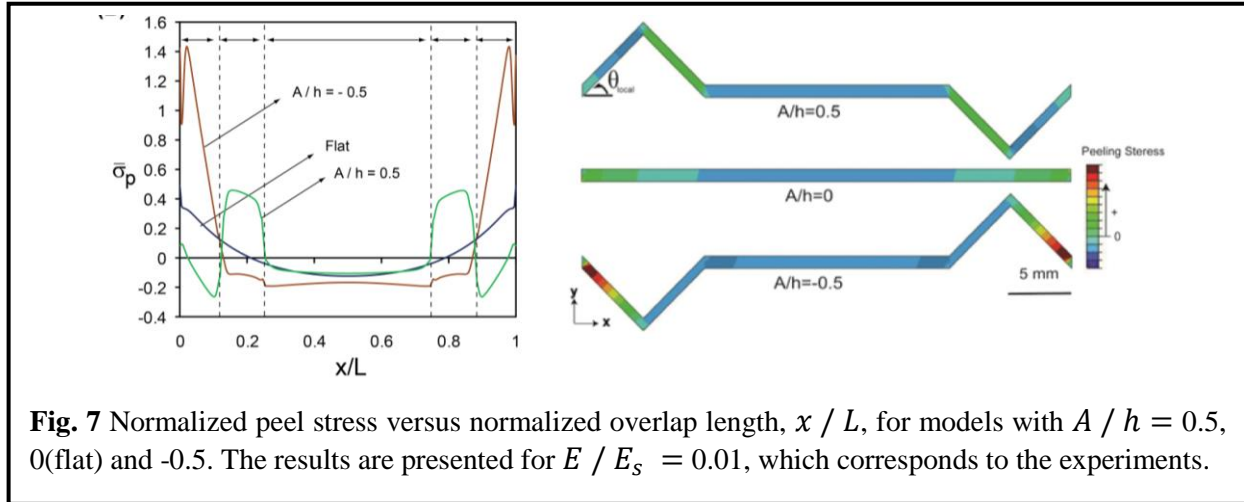esponse, Fig. 6. Directly after this second peak the two initial cracks in regions II link up in region I, overload the remaining bonded regions III and cause sudden specimen breakage. For '∨' specimens, the initial cracks develop and propagate quickly at very low loads in regions III of the bonded interface, causing a small drop in the associated force-displacement curve. However, the cracks arrest at the tooth tip connecting regions III and II, and no crack growth is observed for a relatively large span of further loading. It may be noted that essentially the same behavior would be expected if no adhesive were placed in regions III. In other words, the end segments of the '∨' bond appear to be insignificant to the load capacity and response, and could perhaps be dispensed with in order to eliminate the initial failure stage and associated drop in load.

Although the experimentally evaluated non-flat specimen geometries did not exhibit substantial improvement in ultimate joint strength, the results demonstrate that interface morphology has a significant influence on the overall behavior, and suggest that certain non-flat geometries could be much stronger. Another important aspect of behavior is energy absorption. Considering the overall behavior of bonded joints, flat and '∧' specimens show somewhat less-tough macroscopic behavior, where the occurrence of initial cracking is followed rapidly by overall breakage and sudden loss of load carrying capacity. In contrast, the response of '∨' specimens resembles the *ductile* behavior of most metals, where initial failure causes only a slight reduction in resisting force of the bonded joint. Further elongation results in an increase in load-carrying capacity of the specimen up to the point of failure. In fact, the overall response of '∨' specimens after the initial cracking is regulated by plastic hinging of the metallic adherends at the two peaks of the zigzag interface profile, and is accompanied by significant plastic deformation and rotation of the bonded region prior to overall breakage. (In contrast, the stresses in the metallic adherends of the flat and '∧' specimens never reach yield.)

3.2 Numerical Investigations

Computational analysis of single-lap adhesively bonded joints was performed using the FE analysis software ABAQUS. Adherends and adhesives were modeled as homogeneous isotropic linear elastic materials, with properties given in section 3.1. No failure criteria were incorporated in the analysis, but computed average peel stress normal to adhesive-adherent interface was used to predict the failure (i.e. crack) initiation. Four-node plane stress elements with reduced integration (three degrees of freedom at each node and quadratic shape functions)

Fig. 7 Normalized peel stress versus normalized overlap length, x / L, for models with $A / h = 0.5$, 0(flat) and -0.5. The results are presented for $E / E_s = 0.01$, which corresponds to the experiments.
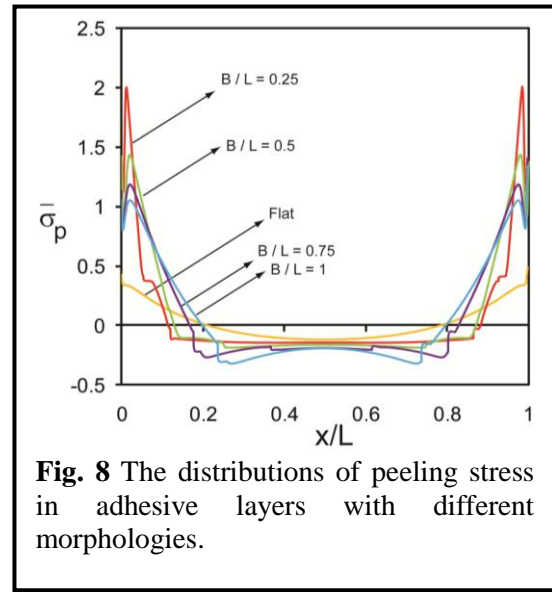
were used for meshing. One end of the modeled specimen was fixed (clamped boundary condition), while the other end was constrained to translate axially parallel to the bond plane, and loaded with an axial force F. In the numerical simulations, total overlap length L of the bond, total specimen length, height h of the specimen, and thickness t of the adhesive were kept constant. Varied quantities included geometric parameters such as tooth height and width, adhesive Young's modulus, and length of sections of interface with no bonding to simulate existence of crack.

The finite element analysis provides an estimate of the elastic stress distribution in the bonded joint. As one way to estimate peel (i.e., normal) and shear stresses in the adhesive, computed stress components at corresponding upper and lower adhesive boundary mesh points are averaged to give 'mean adhesive layer stresses': σ_{xx}, σ_{yy} and σ_{xy}. The computed stress results were normalized by the applied far-field adherend tensile stress, and presented in non-dimensional form as $\bar{\sigma}$ and $\bar{\tau}$, respectively.

In the first set of calculations, only the three specific experimental geometries ($A / h = 0.5$, 0, - 0.5) were simulated. For each, the averaged shearing stress (tangential to the adhesive-adherend interface) and peeling stress (normal to the interface) were obtained all along the bonded joint, as shown in Figures 7 for the peeling stress distribution. The spatial distributions of non-averaged shear and peel stresses within the adhesive are also plotted. This reveals that the elastic stress distribution in the adhesive layer is substantially different in the three specimens, being strongly affected by interface slope and slope discontinuities.
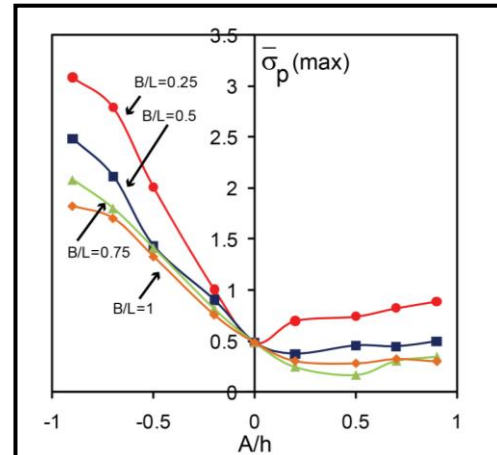
In both non-flat cases, the maximum tensile peel stress is significantly higher than the maximum shear stress. For models with $A / h = 0.5$, the maximum tensile peel stress of 0.45 times the remote tensile stress occurs in regions II, where the initial cracking was observed in our experiments. Peel stress in region III is mainly compressive, so failure is not expected to initiate in this region.

Fig. 8 The distributions of peeling stress in adhesive layers with different morphologies.
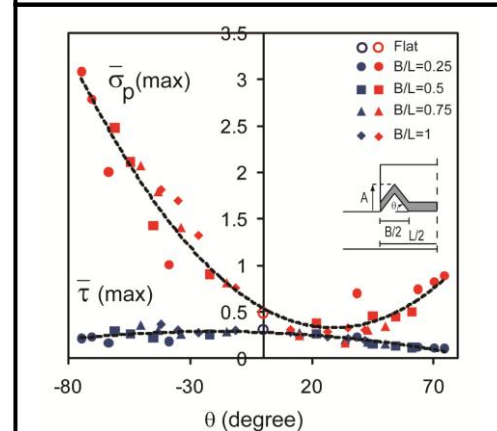
To understand the effect of varying parameters on the distribution of stresses throughout the adhesive, also on performance and load capacity of non-flat bonded joints, we carried out an extensive parametric study. Figure 8 shows a selected set of results related to the distribution of normalized peel stress along the projected adhesive path for non-flat joints with various ratios of total tooth width to total projected bond length, B / L, and tooth height to adherent height ratio of $A/h = -0.5$. Results for the flat joint are plotted for comparison. Stresses vary only gently in the flat regions of all bonded joints. The non-flat joints have lower maximum shear stresses compared to the flat joint, with the lowest maximum shear stress occurring for the joint with $B / L = 0.25$. The peel stress distribution varies significantly for both sets of non-flat bonded joints, showing smaller values for the bonded joints with positive A / h.

Figure 9 is a plot of the maximum peel stress as a function of A / h for bonded joints with various ratios of total tooth width to total projected bond length, B / L. Increasing the tooth width generally leads to smaller values of maximum peel stress in the bonded joint. For negative A / h, the curve for $B / L = 1$ is the lowest, and in fact having no 'flat' area guarantees low peel stress in general. The specific case exhibiting the very lowest peak peel stress is a green triangle at $B / L = 0.75$ and $A / h = 0.5$, with a peak normalized peel stress of about 0.17, which is less than 25% that of the experimental '/\' specimens. Such a geometry should exhibit an estimated fourfold of improvement in strength over the strongest tested specimens.

Based on the results presented above, we can see that increasing B / L or decreasing A / h in general results in the same trend of decreasing stress, and recognize that both of these changes also decrease θ. In Figure 10, we have replotted all results for normalized maximum peel and shear stress against θ. The data are presented for joints with four different non-dimensional tooth width $B / L = 0.25, 0.5, 0.75$ and different amplitudes, representing a wide range of values for tooth angle, θ. Evidently, angle θ is the primary determinant of peak stresses in the bonded joint. The dashed lines in Fig. 10 show the best fit to the data points shown. These lines can be used for estimating the values of maximum stresses in non-flat joint with different configurations. From the results, it can be surmised that a θ value between 10 and 35 degrees leads to small stresses and thus, could be a good design choice. It is noteworthy that the results presented here

Fig. 9 Normalized maximum peel stress in the bonded joint versus A / h for joints with different, B / L.

Fig. 10 Normalized maximum shear and peel stress at adhesive versus the starting angle θ for different geometry ratio.

are for bonded joints subjected to uniaxial tension. However, the significant role of interface morphology on regulating the stress distribution along the bonded joints observed here should be valid for other loading conditions and pertinent to other bonded joint configurations and designs (e.g. double lap joint).

4. Self-Similar Hierarchical Honeycombs

Two-dimensional cellular structures have found widespread application for thermal isolation, energy absorption, structural protection, and as the core of lightweight sandwich panels [64-70]. However, the in-plane properties (e.g. stiffness, strength and energy absorption) of such structures are generally far inferior to their out-of-plane properties. Therefore, cellular structures with modified morphology and organization, such as hierarchical [71, 72] and functionally graded structures [73-75] (with varying wall thickness or cell size) have been developed to improve the in-plane mechanical response. In this part of the project, a hierarchical family of honeycomb-based cellular structures was constructed by systematic introduction of successively smaller hexagonal cells wherever three cell walls meet. This class of hierarchical honeycombs was shown to be capable of attaining superior in-plane modulus to mass ratio (i.e. specific modulus). Analytical and numerical investigations were carried out to investigate the in-plane plastic collapse mechanisms and strength of hierarchical honeycomb at one order of hierarchy, for arbitrary biaxial in-plane loading in principal structural directions. The analysis was based on a lower bound strength estimate from elastic analysis of a unit cell, and also on an upper bound estimate from competing plastic hinge mechanisms defined for the unit cell. To establish the validity of the analytical models, we also carried out two sets of finite element simulations of the unit cell, using beam elements with elastic-perfectly plastic moment-curvature behavior. Next, an extensive numerical investigation was performed to study the in-plane stiffness and plastic collapse strength of hierarchical honeycombs with up to four orders of hierarchy. A wide range of specific stiffness and specific strength can be achieved by changing the architecture of honeycombs. The results provide new insight into the relationship between the structural organization and mechanical behavior of cellular-based materials and lattice structures and suggest novel avenues for creating low density materials with desired properties and function.
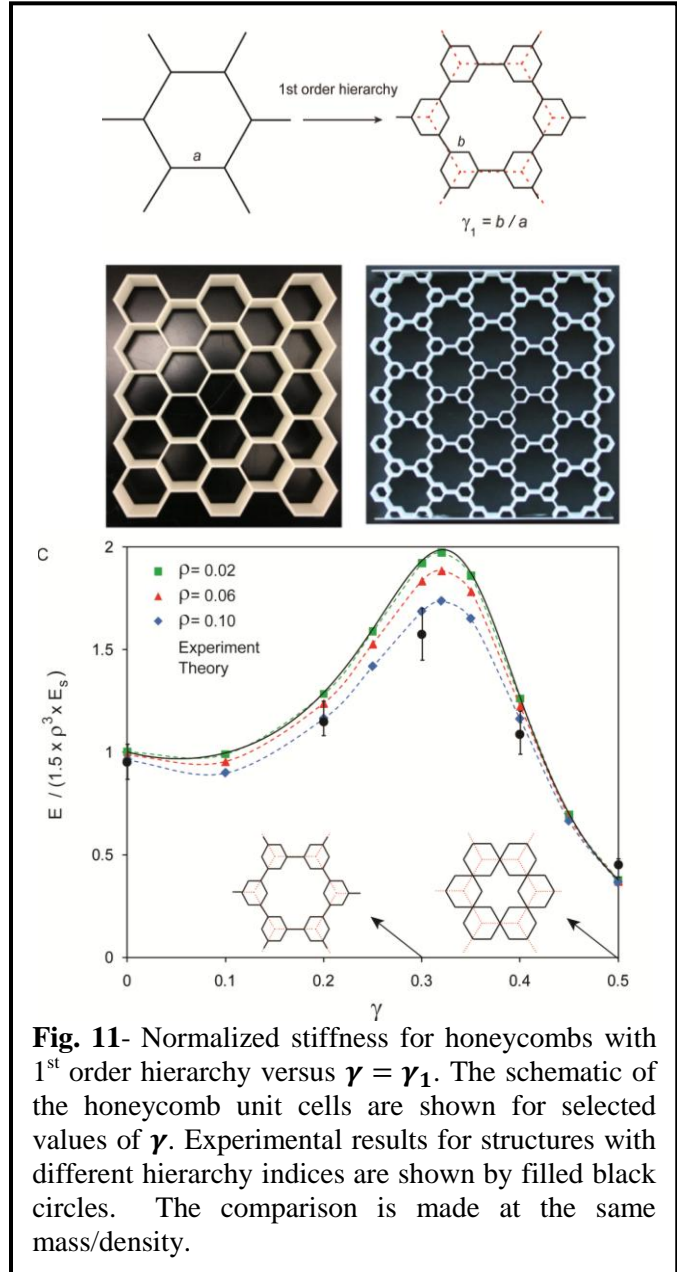
4.1 Experimental Investigations

The hierarchical honeycomb samples were fabricated using 3D printing. Figure 11 (top) shows samples of regular and hierarchical honeycombs with $\rho = 0.10$ and $a = 20$ mm fabricated using 3D printing (Dimensions 3D printer, Stratasys Inc., Eden Prairie, MN). The regular honeycomb has $t = 1.75$mm; the honeycomb with one-level hierarchy has $\gamma_1 = 0.3$ and $t = 1$mm; and that with two-level hierarchy has $\gamma_1 = 0.3$, $\gamma_2 = 0.12$, and $t = 0.75$mm. These were printed as three-dimensional extruded shells from an ABS polymer (acrylonitrile butadiene styrene, elastic modulus = 2.3 GPa) as the bulk material. The input file to the 3D printing software was created for honeycombs with a relative density of 0.10. The cell wall thickness was reduced for honeycombs with hierarchy in order to keep the overall relative density constant, similar to the finite element calculations. The actual printed samples did not maintain the target density very precisely due to the 0.25 mm resolution of the printer (so the relative density was between 8-12%, and only certain discrete values of γ_1 and γ_2 could be achieved). Prior to the experiments, aluminum plates were bonded to the top and bottom of the samples using cyanoacrylate adhesive, in order to prevent the edge nodes from excessive bending. The in-plane compressive response of these bonded-end samples was measured using an INSTRON 5582 at the slow rate of 1mm/min. The effective elastic modulus of the honeycombs were estimated from the slope of the force-displacement curve at early stage of the experiment ($\varepsilon < 1.5\%$). For each specimen, the true relative density was measured by weighing, and then was used when calculating the normalized effective elastic modulus. For each configuration, three samples were tested. In

addition to the experiments, we developed analytical and finite element models to calculate the effective in-plane elastic constants of the honeycombs in terms of cell-wall Young's modulus.

4.2 Analytical Modeling and Numerical Estimation of Stiffness

The deformation of the unit cell of honeycombs with one level of hierarchy under uniaxial loading was estimated using Castigliano's second theorem. Considering symmetry, equilibrium and the relationship between the reaction forces and moments, the effective stiffness of the hierarchical structure, E, can be obtained as $E/E_s = (t/a)^3 f(\gamma_1)$, where $f(\gamma_1) = 40\sqrt{3}/(116\gamma_1^3 + 144\gamma_1^2 - 141\gamma_1 + 30)$. $\gamma_1 = 0$ yields the classical results for regular honeycombs. The comparison between the theoretical data, finite element analysis and experiments is shown in bottom of Fig. 11. The comparison was made at constant overall mass or relative density. The stiffest configuration can be obtained theoretically when $\partial(E/E_s)/\partial\gamma_1 = 0$, which shows that a honeycomb with 1st order of hierarchy and $\gamma_1 = 0.32$ is approximately 2 times stiffer than its regular-honeycomb counterpart. We carried out a similar study for a honeycomb with 2nd order hierarchy, which shows a factor of 3.5 enhancement in stiffness compared to the regular honeycomb [76]

Fig. 11- Normalized stiffness for honeycombs with 1st order hierarchy versus $\boldsymbol{\gamma} = \boldsymbol{\gamma_1}$. The schematic of the honeycomb unit cells are shown for selected values of $\boldsymbol{\gamma}$. Experimental results for structures with different hierarchy indices are shown by filled black circles. The comparison is made at the same mass/density.
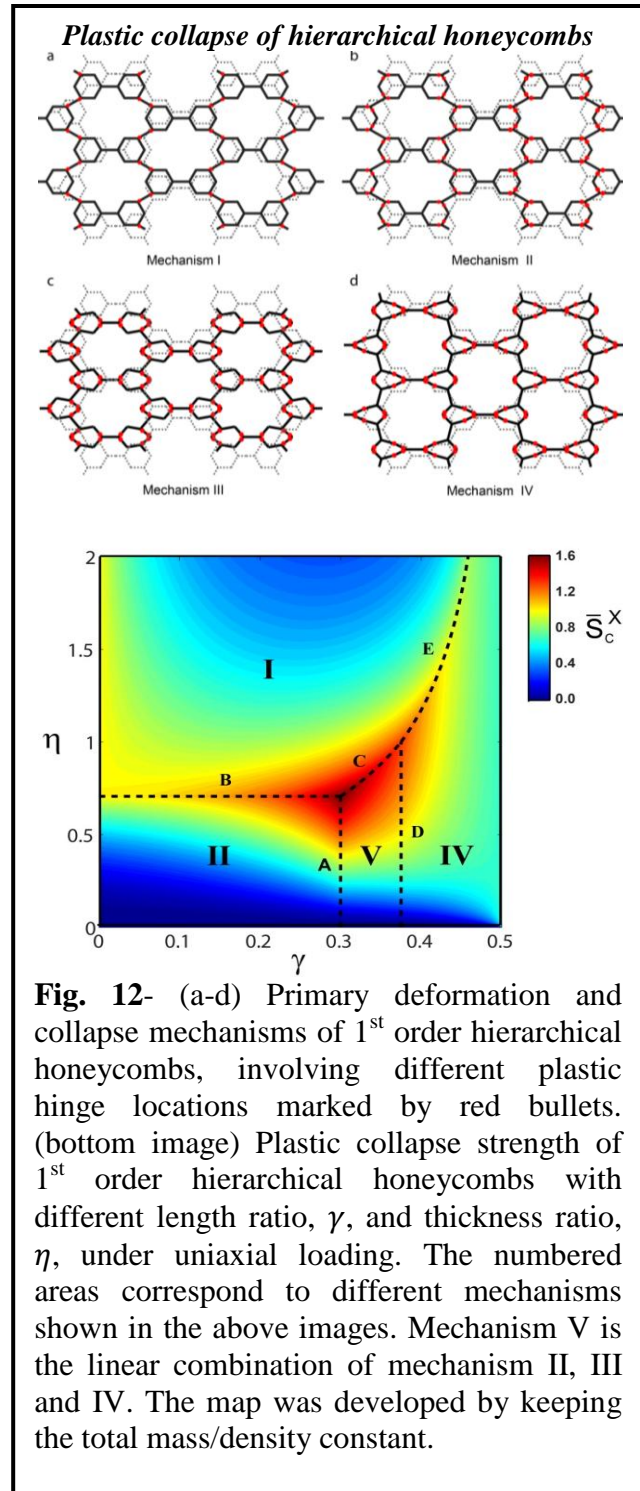
4.3 Analytical Modeling and Numerical Estimation of Stiffness

Figure 12 shows the primary collapse and deformation mechanism of 1st order hierarchical honeycombs with different length ratio, γ, and thickness ratio, η, under uniaxial loading. The plastic collapse strength results, after being normalized by the collapse strength of regular honeycomb of equal density (denoted by $\bar{S}_c^x$) are also plotted. Compared to regular honeycomb, the plastic collapse strength of 1st order hierarchical honeycomb of uniform thickness shows a maximum normalized value of 1.3 in uniaxial loading, occurring at $\gamma = 0.375$. The maximum normalized plastic collapse load, $\bar{S}_c^x = 1.6$, occurs at the optimal values of $\gamma = 0.3$ and $\eta = 1/\sqrt{2} \approx 0.71$, where curves A, B and C join. Studying stiffness and strength of the proposed hierarchical honeycomb, shows that the resulting structure can exhibit many

possible stiffness-strength properties relative to regular honeycomb of same mass, including (stiffer/stronger), (stiffer/weaker), and (more compliant/weaker) properties. Thus, hierarchical honeycombs with self-similar topology could provide new avenues for the development of novel materials and structures with desirable and actively tailorable properties.

Motivated by the increasing trend in the maximum values of stiffness and collapse strength observed for 1st order honeycombs in comparison with the counterpart regular honeycombs, we extended our study to higher order honeycombs. The analytical estimation of plastic collapse strength was not practical because of the increase in the number of possible mechanisms of collapse caused by introducing additional beams for each level of hierarchy. Instead, the finite element method was used on honeycomb unit cells to simulate the plastic collapse of honeycombs with perfectly-plastic material properties. Finite element models with varying geometries were created in MATLAB, and were solved using ABAQUS. Figures 13 shows maps of normalized collapse strength versus normalized stiffness for regular, 1st, 2nd, 3rd and 4th order honeycombs of uniform thickness in x direction, obtained from the finite element analysis. It should be noted that a nth order hierarchical honeycomb is a special configuration of honeycombs with higher order of hierarchy. For example, a 2nd order hierarchical honeycomb is a special configuration of 3rd order hierarchical honeycombs with, $\gamma_3 = 0$. Thus, the entire colored area in Fig. 13 displays the range of achievable stiffness and strength with introducing four orders of hierarchy in the architecture of a regular honeycomb. The

Fig. 12- (a-d) Primary deformation and collapse mechanisms of 1st order hierarchical honeycombs, involving different plastic hinge locations marked by red bullets. (bottom image) Plastic collapse strength of 1st order hierarchical honeycombs with different length ratio, γ, and thickness ratio, η, under uniaxial loading. The numbered areas correspond to different mechanisms shown in the above images. Mechanism V is the linear combination of mechanism II, III and IV. The map was developed by keeping the total mass/density constant.
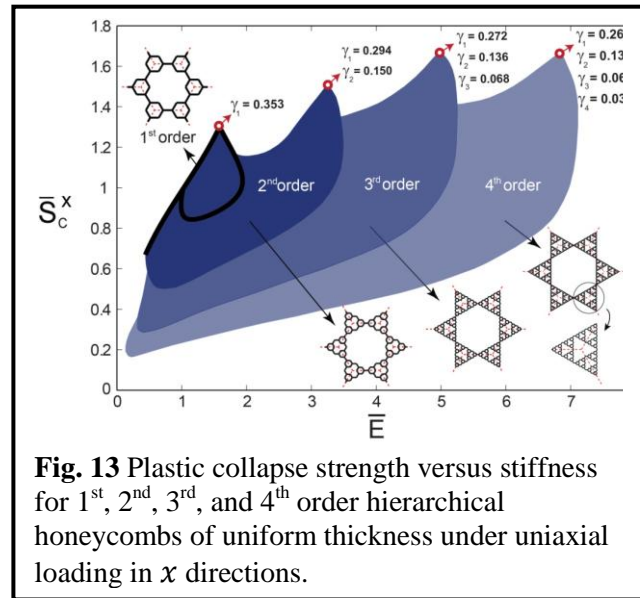
graphs show the large increase in the achievable range of stiffness and plastic collapse strength permitted by increasing the order of hierarchy. The enhancement in the normalized stiffness is more noticeable with the maximum normalized stiffness increasing from 2 and 3.5 for 1st and 2nd order hierarchical honeycombs to 5.3 and 7.1 for 3rd and 4th order hierarchical honeycombs. The maximum value of plastic collapse strength experiences an increase of [30%, 50% and 68%] in x

for [1st, 2nd and 3rd] orders of hierarchy in comparison with a regular honeycomb of the same mass. Introducing the 4th order of hierarchy does not result in significant increase in the maximum normalized strength in either loading condition.

The findings of this study therefore suggest new avenues for the development of novel materials and structures with desirable and perhaps actively tailorable properties. Another goal of the current work is to explore a specific example of hierarchical refinement, in order to identify strategies and their implications. The resulting property increases are viewed as a potential 'driving force' for hierarchical refinement in nature, or in other kinds of structures.

Fig. 13 Plastic collapse strength versus stiffness for 1st, 2nd, 3rd, and 4th order hierarchical honeycombs of uniform thickness under uniaxial loading in x directions.

References:

1. Vincent, J.F.V. and J.D. Currey, *Mechanical properties of biological materials,* 1980, Cambridge, UK: society for experimental biology.
2. Vincent, J.F.V., *Structural biomaterials*1990, Princeton NJ: Princeton University Press.
3. Ruibal, R. and V. Ernst, *The structure of the digital setae of lizards.* Journal of Morphology, 1965. **117**(3): p. 271-293.
4. Arzt, E., S. Gorb, and R. Spolenak, *From micro to nano contacts in biological attachment devices.* Proceedings of the National Academy of Sciences, 2003. **100**(19): p. 10603-10606.
5. Huey, R.B. and P.E. Hertz, *Effects of body size and slope on acceleration of a lizard (Stellio stellio).* Journal of Experimental Biology, 1984. **110**(1): p. 113-123.
6. Russell, A.P., *A contribution to the functional analysis of the foot of the Tokay, Gekko gecko (Reptilia: Gekkonidae).* Journal of Zoology, 1975. **176**(4): p. 437-476.
7. Hu, D.L., B. Chan, and J.W. Bush, *The hydrodynamics of water strider locomotion.* Nature, 2003. **424**(6949): p. 663-666.
8. Foelix, R., *Biology of spiders*2010: Oxford University Press.
9. Wigglesworth, V., *How does a fly cling to the under surface of a glass sheet?* Journal of Experimental Biology, 1987. **129**(1): p. 373-376.
10. Sarikaya, M. and I. Aksay, *Biomimetics: design and processing of materials*1995: AIP Press.
11. Currey, J.D., *Mechanical Properties of Mother of Pearl in Tension.* Proceedings of the Royal Society of London. Series B, Biological Sciences, 1977. **196**(1125): p. 443-463.
12. Jackson, A.P., J.F.V. Vincent, and R.M. Turner, *The Mechanical Design of Nacre.* Proceedings of the Royal Society of London. Series B, Biological Sciences, 1988. **234**(1277): p. 415-440.
13. Wang, R., et al., *Deformation mechanisms in nacre.* J. Mater. Res, 2001. **16**(9): p. 2485-2493.

14. Menig, R., et al., *Quasi-static and dynamic mechanical response of< i> Haliotis rufescens</i>(abalone) shells.* Acta Materialia, 2000. **48**(9): p. 2383-2398.

15. Wang, R., et al., *Observations of damage morphologies in nacre during deformation and fracture.* Journal of materials science, 1995. **30**(9): p. 2299-2304.

16. Li, X., et al., *Nanoscale Structural and Mechanical Characterization of a Natural Nanocomposite Material: The Shell of Red Abalone.* Nano Letters, 2004. **4**(4): p. 613-617.

17. Kotha, S., Y. Li, and N. Guzelsu, *Micromechanical model of nacre tested in tension.* Journal of materials science, 2001. **36**(8).

18. Katti, K.S., et al., *Platelet interlocks are the key to toughness and strength in nacre.* Journal of Materials Research, 2005. **20**(05): p. 1097-1100.

19. Hadley, N., *The arthropod cuticle.* Scientific American 1986. **255**(1): p. 98-106.

20. Factor, J.R., *Biology of the Lobster Homarus americanus*, in *Academic Press*1995.

21. Horst, M.N. and J.A. Freeman, *The Crustacean Integument, Morphology and Biochemistry*1993, Ann Arbor, MI: CRC Press.

22. Pokroy, B., et al., *Fabrication of bioinspired actuated nanostructures with arbitrary geometry and stiffness.* Advanced Materials, 2009. **21**(4): p. 463-469.

23. Munch, E., et al., *Tough, Bio-Inspired Hybrid Materials.* Science, 2008. **322**(5907): p. 1516-1520.

24. Bonderer, L.J., A.R. Studart, and L.J. Gauckler, *Bioinspired Design and Assembly of Platelet Reinforced Polymer Films.* Science, 2008. **319**(5866): p. 1069-1073.

25. Khademhosseini, A., et al., *Microscale technologies for tissue engineering and biology.* Proceedings of the National Academy of Sciences of the United States of America, 2006. **103**(8): p. 2480-2487.

26. Dillow, A.K. and A.M. Lowman, *Biomimetic materials and design: biointerfacial strategies, tissue engineering and targeted drug delivery*2002: CRC Press.

27. Mahdavi, A., et al., *A biodegradable and biocompatible gecko-inspired tissue adhesive.* Proceedings of the National Academy of Sciences, 2008. **105**(7): p. 2307-2312.

28. Hansen, W. and K. Autumn, *Evidence for self-cleaning in gecko setae.* Proceedings of the National Academy of Sciences of the United States of America, 2005. **102**(2): p. 385-389.

29. Kim, T.i., et al., *Stooped Nanohairs: Geometry‐Controllable, Unidirectional, Reversible, and Robust Gecko‐like Dry Adhesive.* Advanced Materials, 2009. **21**(22): p. 2276-2281.

30. Sun, W., et al., *The nature of the gecko lizard adhesive force.* Biophysical journal, 2005. **89**(2): p. L14-L17.

31. Delamarche, E., et al., *Stability of molded polydimethylsiloxane microstructures.* Advanced Materials, 1997. **9**(9): p. 741-746.

32. Kim, S. and M. Sitti, *Biologically inspired polymer microfibers with spatulate tips as repeatable fibrillar adhesives.* Applied Physics Letters, 2006. **89**(26): p. 261911-261911-3.

33. Murphy, M.P., B. Aksak, and M. Sitti, *Gecko‐Inspired Directional and Controllable Adhesion.* Small, 2009. **5**(2): p. 170-175.

34. Aksak, B., M.P. Murphy, and M. Sitti, *Adhesion of biologically inspired vertical and angled polymer microfiber arrays.* Langmuir, 2007. **23**(6): p. 3322-3332.

35. Lee, J., R.S. Fearing, and K. Komvopoulos, *Directional adhesion of gecko-inspired angled microfiber arrays.* Applied Physics Letters, 2008. **93**(19): p. 191910-191910-3.

36. Murphy, M.P., B. Aksak, and M. Sitti, *Adhesion and anisotropic friction enhancements of angled heterogeneous micro-fiber arrays with spherical and spatula tips.* Journal of Adhesion Science and Technology, 2007. **21**(12-13): p. 1281-1296.

37. Qu, L., et al., *Carbon nanotube arrays with strong shear binding-on and easy normal lifting-off.* Science, 2008. **322**(5899): p. 238-242.

38. Geim, A., et al., *Microfabricated adhesive mimicking gecko foot-hair.* Nature Materials, 2003. **2**(7): p. 461-463.

39. Lee, H., B.P. Lee, and P.B. Messersmith, *A reversible wet/dry adhesive inspired by mussels and geckos.* Nature, 2007. **448**(7151): p. 338-341.

40. Reddy, S., E. Arzt, and A. del Campo, *Bioinspired surfaces with switchable adhesion.* Advanced Materials, 2007. **19**(22): p. 3833-3837.

41. Chan, E.P., et al., *Surface wrinkles for smart adhesion.* Advanced Materials, 2008. **20**(4): p. 711-716.

42. Wood, R.J., *The first takeoff of a biologically inspired at-scale robotic insect.* Robotics, IEEE Transactions on, 2008. **24**(2): p. 341-347.

43. Hu, D.L., et al., *Water-walking devices.* Experiments in Fluids, 2007. **43**(5): p. 769-778.

44. Lee, J., et al., *Sliding-induced adhesion of stiff polymer microfibre arrays. I. Macroscale behaviour.* Journal of The Royal Society Interface, 2008. **5**(25): p. 835-844.

45. Autumn, K., et al., *Frictional adhesion: a new angle on gecko attachment.* Journal of Experimental Biology, 2006. **209**(18): p. 3569-3579.

46. Yao, H., et al., *Adhesion and sliding response of a biologically inspired fibrillar surface: experimental observations.* Journal of The Royal Society Interface, 2008. **5**(24): p. 723-733.

47. Davis, M. and D. Bond, *Principles and practices of adhesive bonded structural joints and repairs.* International journal of adhesion and adhesives, 1999. **19**(2): p. 91-105.

48. Kinloch, A., *Interfacial fracture mechanical aspects of adhesive bonded joints—a review.* 1979.

49. Sheppard, A., D. Kelly, and L. Tong, *A damage zone model for the failure analysis of adhesively bonded joints.* International journal of adhesion and adhesives, 1998. **18**(6): p. 385-400.

50. Xiong, J., et al., *Mechanical behavior and failure of composite pyramidal truss core sandwich columns.* Composites Part B: Engineering, 2011.

51. Banea, M. and L. Da Silva, *Adhesively bonded joints in composite materials: an overview.* Proceedings of the Institution of Mechanical Engineers, Part L: Journal of Materials Design and Applications, 2009. **223**(1): p. 1-18.

52. Renton, W.J. and J.R. Vinson, *The efficient design of adhesive bonded joints.* The Journal of Adhesion, 1975. **7**(3): p. 175-193.

53. Katsiropoulos, C.V., et al., *Fracture toughness and shear behavior of composite bonded joints based on a novel aerospace adhesive.* Composites Part B: Engineering, 2012. **43**(2): p. 240-248.

54. Zeng, Q.G. and C. Sun, *Novel design of a bonded lap joint.* AIAA journal, 2001. **39**(10): p. 1991-1996.

55. Avila, A.F. and P.O. Bueno, *Stress analysis on a wavy-lap bonded joint for composites.* International journal of adhesion and adhesives, 2004. **24**(5): p. 407-414.

56.   Shiva Shankar, G., S. Vijayarangan, and N. Krishna. *Failure Analysis of Lap and Wavy-lap Composite Bonded Joints*. in *International Symposium of Research Students on Materials Science and Engineering*. 2004.

57.   Ashrafi, M., et al., *Adhesively bonded single lap joints with non-flat interfaces.* International journal of adhesion and adhesives, 2012. **32**: p. 46-52.

58.   Vaziri, A., H. Nayeb-Hashemi, and H. Hamidzadeh, *Experimental and analytical investigations of the dynamic response of adhesively bonded single lap joints.* Journal of vibration and acoustics, 2004. **126**(1): p. 84-91.

59.   Olia, M. and J. Rossettos, *Analysis of adhesively bonded joints with gaps subjected to bending.* International Journal of Solids and Structures, 1996. **33**(18): p. 2681-2693.

60.   Rossettos, J. and E. Zang, *On the peak shear stresses in adhesive joints with voids.* NASA, 1997(19990018176).

61.   Harris, J. and R. Adams, *Strength prediction of bonded single lap joints by non-linear finite element methods.* International journal of adhesion and adhesives, 1984. **4**(2): p. 65-78.

62.   Her, S.C., *Stress analysis of adhesively-bonded lap joints.* Composite structures, 1999. **47**(1): p. 673-678.

63.   Vaziri, A. and H. Nayeb-Hashemi, *Dynamic response of tubular joints with an annular void subjected to a harmonic axial load.* International Journal of Adhesion and Adhesives, 2002. **22**(5): p. 367-373.

64.   Gu, S., T.J. Lu, and A.G. Evans, *On the design of two-dimensional cellular metals for combined heat dissipation and structural load capacity.* International Journal of Heat and Mass Transfer, 2001. **44**(11): p. 2163-2175.

65.   Lu, T.J., H.A. Stone, and M.F. Ashby, *Heat transfer in open-cell metal foams.* Acta Materialia, 1998. **46**(10): p. 3619-3635.

66.   Wadley, H.N.G., N.A. Fleck, and A.G. Evans, *Fabrication and structural performance of periodic cellular metal sandwich structures.* Composites Science and Technology, 2003. **63**(16): p. 2331-2343.

67.   Wadley, H.N.G., *Multifunctional periodic cellular metals.* Philosophical Transactions of the Royal Society A: Mathematical, Physical and Engineering Sciences, 2006. **364**(1838): p. 31-68.

68.   Vaziri, A., Z. Xue, and J.W. Hutchinson, *Performance and failure of metal sandwich plates subjected to shock loading.* Journal of Materials and Structure, 2007. **2**: p. 1947-1963.

69.   Vaziri, A., Z. Xue, and J. Hutchinson, *Metal sandwich plates with polymer foam-filled cores.* Journal of Mechanics of Materials and Structures, 2006. **1**(1): p. 97-127.

70.   Vaziri, A. and J.W. Hutchinson, *Metal sandwich plates subject to intense air shocks.* International Journal of Solids and Structures, 2007. **44**(6): p. 2021-2035.

71.   Ajdari, A., et al., *Hierarchical honeycombs with tailorable properties.* International Journal of Solids and Structures, 2012.

72.   Lakes, R., *Materials with structural hierarchy.* Nature, 1993. **361**(6412): p. 511-515.

73.   Ajdari, A., H. Nayeb-Hashemi, and A. Vaziri, *Dynamic crushing and energy absorption of regular, irregular and functionally graded cellular structures.* International Journal of Solids and Structures, 2011. **48**(3–4): p. 506-516.

74.   Miyoshi, T., et al., *Enhancement of energy absorption in a closed-cell aluminum by the modification of cellular structures.* Scripta materialia, 1999. **41**(10).

75.   Li, K., X.L. Gao, and J. Wang, *Dynamic crushing behavior of honeycomb structures with irregular cell shapes and non-uniform cell wall thickness.* International Journal of Solids and Structures, 2007. **44**(14): p. 5003-5026.

76.   Ajdari, A., et al., *Hierarchical honeycombs with tailorable properties.* International Journal of Solids and Structures, 2012. **49**(11-12): p. 1413–1419.